




Application of the Green's function formalism to the interplay between avalanche and multiphoton ionization induced by optical pulses

Alessandro Alberucci ^{1,*}, Chandroth P. Jisha ¹ and Stefan Nolte ^{1,2}

¹*Institute of Applied Physics, Abbe School of Photonics, Friedrich Schiller University Jena, Albert-Einstein-Str. 15, 07745 Jena, Germany*

²*Fraunhofer Institute for Applied Optics and Precision Engineering IOF, Albert-Einstein-Str. 7, 07745 Jena, Germany*



(Received 21 December 2023; revised 13 March 2024; accepted 22 March 2024; published 10 April 2024)

A fundamental brick of light-matter interaction at large optical intensities is the generation of a plasma. The optically induced plasma in turn plays a fundamental role in determining the optical propagation. The plasma generation is a result of the interplay between multiphoton, tunnel, and avalanche ionization. Here we use the basic rate equations to discuss an analytical model for the interaction between these physical effects. After defining a nonlinear impulse response for the system, we describe how the interplay depends on the features of the optical pulses. Our approach strongly simplifies the modeling of the propagation of ultrashort pulses, paving the way to a much easier and faster interpretation of experimental observations, with potential impact on the broad fields of ultrafast light-matter interaction and laser micromachining.

DOI: [10.1103/PhysRevB.109.144302](https://doi.org/10.1103/PhysRevB.109.144302)

I. INTRODUCTION TO NONLINEAR PHOTOIONIZATION

The interaction of intense optical pulses with matter is a topic of central interest in physics. Indeed, the nonlinear optical regime is intrinsically a strongly out-of-equilibrium system due to the rapidity in the exchange of energy between the electromagnetic field and the atoms [1,2]. This allows the experimental investigation of new regimes in condensed matter physics, including many-body problems and Floquet systems [3,4] or the measurement of the material properties, using, for example, high harmonic generation [5–7]. Beyond the basic physics, the problem is of primary importance because strong lasers can modify the properties of a material in a temporary manner [2,6] or by inducing permanent modifications, a phenomenon widely exploited in laser micromachining [8,9].

One common feature of the interaction between intense light and matter is the formation of plasma [10,11]. The impinging photons provide energy to the electrons of the material, thus inducing a considerable amount of electronic transitions towards higher energy states. This process takes place even in materials which are transparent in the linear regime due to the tunnel ionization (TI) [12] and multiphoton ionization (MPI) [13]. Once free carriers are generated, the optical field is accelerating them, on average providing an increase in the kinetic energy. The accelerated electrons can then collide with other less energetic electrons, inducing a field-dependent and concentration-dependent amplification. Such an effect is called avalanche ionization (AI), and it is often associated with the dielectric breakdown [14].

On theoretical grounds, the problem of the strong coupling between light and matter can be solved quantum mechanically using Time-Dependent Density Functional Theory [15], yet

a very demanding approach from a computational point of view. At a larger scale, the dynamics of the sea of electrons subject to an optical field can be solved using the machinery of the Boltzmann's transport equations [16]. In most cases, this method is prohibitive given it requires the full knowledge of the energy dispersion for the electrons and of the loss mechanisms (e.g., excitons and electron-phonon coupling). A common and prolific approach is to define a distribution for the excited electrons $n_e(\mathbf{r}, t)$ averaged over the energetic and momentum states, thus depending only on space and time. This approximation works well in a wide range of materials, including liquids [17], amorphous solids [18], and semiconductors [19]. Neglecting electron diffusion in space, n_e is then dictated by the rate equation [13,20,21]

$$\frac{\partial n_e}{\partial t} = W_{\text{PI}}(I) + \left(\alpha_{\text{av}} I - \frac{1}{\tau_{\text{el}}} \right) n_e - \sigma n_e^2. \quad (1)$$

In Eq. (1) $I(\mathbf{r}, t)$ is the optical intensity of a field with central frequency ω . The first term on the right-hand side (r.h.s.) W_{PI} is the photoionization rate (PI) as predicted by Keldysh's theory for atomic transitions under the influence of a periodic field [13,22]; the second term on the r.h.s. $\alpha_{\text{av}} I n_e$ accounts for the electrons excited by the avalanche effect [14,21]; the third term $-n_e/\tau_{\text{el}}$ accounts for the average lifetime of the excited electrons due to the various recombination mechanisms. Finally, the last term proportional to the square of the density represents the nonlinear (with respect to the electron density n_e) recombination effects, such as Auger.

Keldysh's theory is amazingly capable of modeling both tunneling and multiphoton ionization: the transition between the two regimes is demarcated by the so-called Keldysh parameter $\gamma \propto \frac{\omega}{q} \sqrt{mc n \epsilon_0 E_g / I}$, where E_g is the band gap of the material, c is the speed of light, ϵ_0 is the vacuum dielectric permittivity, and finally m and q are the mass and the charge of the electron, respectively [23]. In the MPI case γ is large, in turn

*alessandro.alberucci@uni-jena.de

yielding $W_{\text{PI}} \approx \frac{1}{\hbar\omega} \sum_N \frac{\alpha_N}{N} I^N$, where α_N is the cross section for the ionization involving N photons. As shown below, the type of ionization (TI or MPI) does not significantly change our results, in fact providing only a different mathematical relationship between the optical intensity and the source of electrons. Thus, for simplicity, we will restrict ourselves at first to MPI and neglect TI. At the end of the article we will show how our approach works when the full Keldysh formula is applied. Incidentally, we are for now considering the general case of multiple multiphoton transitions, although usually the smallest one fulfilling $N\hbar\omega \geq E_g$ is the relevant one.

II. SOLUTION VIA THE GREEN FUNCTION FORMALISM

The usage of a rate equation to model the plasma formation in strong optical fields was described by Shen in his seminal book on nonlinear optics [24], and later expanded to its final form by Kennedy in 1995 [17]. More complicated versions introducing different energetic states have been discussed [25,26], but the fundamental physics does not depend strongly on that. Furthermore, as discussed, for example, in Ref. [27], the optical breakdown is usually not strongly affected by σn_e^2 , which can then be neglected. The role of the nonlinear recombination term is discussed in Appendix C. Interestingly, in Ref. [28] an analytic formula for the model including nonlinear recombination terms in the case of square pulses is calculated, thus permitting to assess the relevance played by this recombination term. Under the assumptions made, Eq. (1) is linear with respect to the electronic distribution n_e : it can then be solved using the Green's function formalism [29]

$$n_e(\mathbf{r}, t) = \frac{1}{\hbar\omega} \sum_N \frac{\alpha_N}{N} \int_{-\infty}^{\infty} I^N(\mathbf{r}, t') G(\mathbf{r}, t, t') dt', \quad (2)$$

where the impulse response is

$$G(\mathbf{r}, t, t') = e^{\alpha_{\text{av}} \int_{t'}^t I(\mathbf{r}, \tau) d\tau} e^{-(t-t')/\tau_{el}} u_0(t-t'). \quad (3)$$

In Eq. (3) u_0 is the Heaviside function, necessary to fulfill the causality condition. The Green's function also retains the reciprocity property given that $G(\mathbf{r}, t, t') = G(\mathbf{r}, t', t)$. Equations (2) and (3) are the core of the reasoning and findings we are developing in this paper. In this form and as anticipated earlier, it is clear that the form of the field-induced ionization solely changes the forcing term in Eq. (1), thus not affecting the solution method we are proposing here. As a matter of fact, solutions of Eq. (1) in terms of an integral were already sketched in the original paper by Kennedy [17], and explicitly written by Feng and collaborators in Ref. [27]. Nonetheless, such an integral solution has not been explored in depth to discuss the interplay between MPI and AI; indeed, verbatim from Ref. [27]: "Since the analytic solution (8) is not very informative, we have numerically solved the density equation." Oppositely to the reported view, we show that writing such an integral in terms of the Green's formalism permits us to disclose how field ionization (either MPI or TI) and AI are working together and explore the underlying physical behavior. In Appendix A we also provide the generalization of Eq. (3) to the case where electron diffusion is accounted for in the rate Eq. (1).

III. GENERAL PROPERTIES OF THE SOLUTIONS

The first advantage of our approach is the possibility to clearly distinguish the origin of the excited electrons and how MPI and AI interact with each other. To further simplify the notation, hereafter we will focus on the case when only one single multiphoton transition is relevant: the generalization to multiple simultaneous transitions is straightforward. From Eqs. (2) and (3) the net generation of excited electrons per unit time is

$$\frac{\partial n_e}{\partial t} = \frac{\alpha_N}{N\hbar\omega} \left\{ I^N(t) + \left[\alpha_{\text{av}} I(t) - \frac{1}{\tau_{el}} \right] \int_{-\infty}^t I^N(t') \times e^{\alpha_{\text{av}} \int_{t'}^t I(\tau) d\tau} e^{-(t-t')/\tau_{el}} dt' \right\}. \quad (4)$$

Equation (4) allows immediate physical interpretation: the excitation rate is the sum of the instantaneous MPI (first term on the r.h.s.) plus the avalanche electrons generated at each instant normalized with respect to the lifetime τ_{el} (the integral term). The seed for the avalanche electrons is provided by the MPI at former times, whereas the history of the pulse intensity $I(t)$ determines the overall amplification for each electron generated by MPI. Although Eq. (4) is somehow trivial under our model based upon the temporal Green's function, it cannot be easily extracted from numerical solutions of Eq. (1).

We now turn our attention to describe the type of response modeled through Eq. (3). For the sake of simplicity, hereon we will omit the spatial dependence, which is not relevant in our current discussion. Once a shape for the pulse is fixed, the Green's function depends only on the product $\alpha_{\text{av}} I_0$, where I_0 is the intensity peak. The shape of the response of the material depends on the relative position along the pulse profile [i.e., $G(t, t') \neq G(t-t')$] through the avalanche term; i.e., the response is not invariant with respect to time shifts; accordingly, the distribution n_e is not given by a simple temporal convolution. On a more physical ground, Eq. (2) tells us that n_e at a given instant t is the sum of the electrons excited by MPI at each previous instants, but such electron density needs to be weighted with respect to the amount of amplification—fixed by the net balance between avalanche and losses—the electrons have been subjected to. From Eq. (3), the position t_{max} of the extrema of the Green's function G vs t is

$$I(t_{\text{max}}) = \frac{1}{\tau_{el} \alpha_{\text{av}}}. \quad (5)$$

The causality condition imposes the additional constraint $t_{\text{max}} > 0$. The former equation holds valid irrespective of the temporal shape $I(t)$. Generally speaking, Eq. (5) correctly predicts that, for larger α_{av} or for longer electron lifetime τ_{el} , the maximum of the avalanche-generated electrons shifts towards the trailing edge of the pulse, regardless of when the seed electrons (i.e., t') have been generated.

The fluence is the temporal integral of the intensity I . Defining the time-windowed fluence $F(t_1, t_2)$ as the amount of fluence between the two instants t_1 and t_2 , Eq. (3) provides

$$G(t, t') = \left[1 + \alpha_{\text{av}}^n \sum_{n=1}^{\infty} \frac{F^n(t', t)}{n!} \right] e^{-(t-t')/\tau_{el}} u_0(t-t'). \quad (6)$$

The optical response (free electrons actually change both the imaginary and the real part of the refractive index) of the material can then be controlled by shaping the impinging pulses, with potential applications in the novel field of photonic materials encompassing a time-dependent response [30,31]. Furthermore, as the intensity is ramping up, more terms in Eq. (6) become relevant: the joint action of MPI and AI effectively behaves like a multiphoton ionization of order $N + n$ [32], but encompasses an additional memory effect registering the previous slices of the optical pulses already passed through the material [33].

We now focus on how the MPI and AI interact. Given that Eq. (6) provides the amount of electrons excited by an impulsive pulse placed in $t = t'$, the avalanche process excites more electrons than the MPI once:

$$\lim_{t \rightarrow \infty} F(t', t) > \frac{1}{\alpha_{av}}. \quad (7)$$

This means that the share of AI-excited electrons with respect to the ones ascribed to MPI depends primarily on the fluence which crossed the material after the excitation instant t' . Hence, the shape of the pulse—including the pulse duration τ —determines the (continuous) transition between the two regimes; the transition between MPI and AI occurs at a given instant t' along the optical pulse. When the maximum fluence $F(-\infty, \infty)$ is lower than $1/\alpha_{av}$, MPI remains the dominant mechanism exciting the electrons to the conduction band.

Actually, Eq. (7) alone does not ensure the dominance of AI over MPI in the ionization process. Indeed, AI could be dominant at the front edge of the pulse, where the low intensity generates a modest number of seed electrons via the MPI to be later accelerated by the avalanche process. To assess this matter, we can calculate which instant t' (we dub it t^*) contributes the largest number of electronic transitions. By deriving the integrand of Eq. (2) and setting such time derivative (with respect to t') equal to zero, we find the condition

$$\frac{\partial I}{\partial t} = \frac{\alpha_{av}}{N} I^2 - \frac{I}{N\tau_{el}}. \quad (8)$$

For the sake of simplicity, let us assume a single-humped pulse shape; see Fig. 1 for a graphical solution of the equation [34,35]. Until not otherwise specified, hereafter we will employ dimensionless units to investigate the solutions of Eq. (1); at the end of the paper, we will provide examples in physical units for the sake of comparison with experimental works. The r.h.s. of Eq. (8) needs to be positive to ensure $t^* < 0$ to achieve net gain, thus setting the constraint $I_0 > 1/(\alpha_{av}\tau_{el})$ with I_0 being the maximum intensity. In fact, in the absence of avalanche ($\alpha_{av} = 0$) and for $\tau_{el} \rightarrow \infty$, the maximum of n_e corresponds to the intensity peak. When α_{av} is large enough, the instant t^* moves towards the front edge of the pulse, where the temporal derivative $\partial I/\partial t$ [l.h.s. of Eq. (8)] is nonvanishing and positive; see the red curves in Figs. 1(a)–1(c). Thus, larger intensities enhance the shift of t^* towards earlier instants; the larger the α_{av} the larger the shift is [compare the blue and orange curves in Fig. 1(d)]. Finally, greater N favors the MPI by decreasing the temporal shift of t^* with respect to lower N [compare the blue and green curves in Fig. 1(d)].

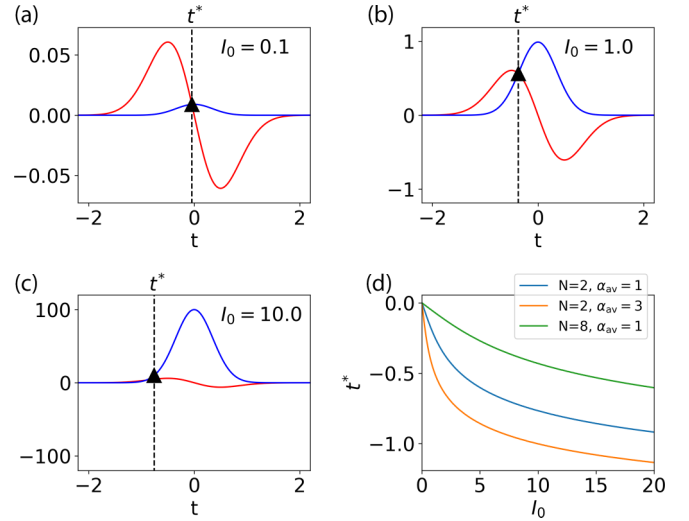


FIG. 1. (a–c) Graphical solution of Eq. (8) for a Gaussian pulse featuring a pulse duration $\tau = 1$ and a peak intensity I_0 equal to 0.1 (a), 1 (b), and 10 (c). Red and blue curves correspond to the left-hand side (l.h.s.) and r.h.s. of Eq. (8), respectively. In (a)–(c) we assumed $\alpha_{av} = 2$. (d) Behavior of t^* vs I_0 for three different pairs of α_{av} and N as labeled in the legend. Here we have fixed $\tau_{el} = 50$.

IV. COMPUTATION FOR SPECIFIC PULSE SHAPES

We now proceed with showing applications of Eqs. (2) and (3) for specific optical pulse shapes: the scope is to demonstrate the versatility of our approach in determining the influence of the pulse shape on the plasma generation. We make the additional assumption that the shape of the optical pulse is fixed: we are thus neglecting self-phase modulation, in both space and time [23]. To be more quantitative and provide closed-form solutions for n_e , we now suppose the pulse to be a square function, $I(t) = I_0 \text{rect}_\tau(t)$, where the rect function is nonvanishing and equal to 1 only for $|t| < \tau/2$. After defining the net gain $g(I_0) = \alpha_{av}I_0 - 1/\tau_{el}$, Eq. (2) with the help of Eq. (6) provides

$$n_e(t) = \frac{\alpha_N I_0^N}{g(I_0) N \hbar \omega} \left\{ \left[e^{g(I_0)(t + \frac{\tau}{2})} - 1 \right] \text{rect}_\tau(t) \right\} + n_e^{\max} e^{-\frac{t - \tau/2}{\tau_{el}}} u_0 \left(t - \frac{\tau}{2} \right). \quad (9)$$

Equation (9) is actually in agreement with the analytical results reported in Ref. [28], where the full recombination Eq. (1) is solved for a square pulse, the equation in turn becoming a Riccati one. In Eq. (9) we also defined the peak of the electron density as

$$n_e^{\max} = \frac{\alpha_N I_0^N}{g(I_0) N \hbar \omega} (e^{g(I_0)\tau} - 1). \quad (10)$$

Numerical simulations confirm the validity of our solution; see Appendix B. The interpretation of Eq. (9) is straightforward: during the pulse the number of electrons grows exponentially with the intensity-dependent net gain $g(I_0)$. The density n_e achieves its maximum n_e^{\max} at the end of the pulse ($t = \tau/2$), then exponentially decays with a lifetime determined by τ_{el} . The interplay between AI and MPI can be evaluated by expanding the exponential term in Eq. (10)

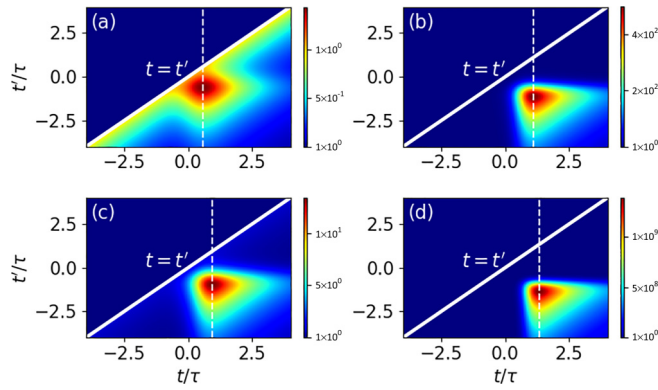


FIG. 2. Green's function for a Gaussian pulse centered in $t = 0$. The pulse duration τ is 1 (a, b) and 3 (c, d). The avalanche amplification is 1 (a, c) and 6 (b, d), whereas we fixed $I_0 = 1$ and $\tau_{el} = 2\tau$ in all the panels. Vertical dashed lines is the maximum position according to Eq. (12).

in its power series. At low gains ($g(I_0)\tau \ll 1$), we obtain $n_e^{\max} = \alpha_N I_0^N \tau / (N\hbar\omega)$, i.e., the case of electrons generated only by MPI. In the opposite limit $g(I_0)\tau \gg 1$, we have a purely exponential growth of the first electrons generated at the leading edge of the pulse, $n_e^{\max} \propto W_{PI}|_{t=-\tau/2} e^{g(I_0)\tau} / g(I_0)$. For the intermediate case we expand the exponential series up to the quadratic terms, providing the following condition for the transition to an avalanche-dominated ionization:

$$\alpha_{av} I_0 > \frac{2}{\tau} + \frac{1}{\tau_{el}}, \quad (11)$$

in agreement with Eq. (8).

Thus, in the case of square pulses the transition between MPI and AI does not depend on the transition order N : the shortest between the pulse duration τ and the electron lifetime τ_{el} is actually determining the transition between the two regimes. In agreement with the numerical simulations of Eq. (1), AI becomes dominant after a given threshold intensity dependent on the pulse duration, with shorter pulses favoring MPI. Finally, from Eq. (10) it is expected that the nonlinear absorption increases as I_0^N for small enough intensities, then depending as I_0^{N+1} when AI kicks in, finally going to a full exponential increase when AI is largely dominant. This general trend is upper bounded in real experiments by the optical breakdown and permanent modifications induced in the material.

We now pass to the most common case of a Gaussian-shaped pulse, $I = I_0 e^{-2t^2/\tau^2}$. The function F is then $F(t, t') = \frac{I_0 \tau}{2} \sqrt{\frac{\pi}{2}} [\text{erf}(\frac{\sqrt{2}t}{\tau}) - \text{erf}(\frac{\sqrt{2}t'}{\tau})]$. From Eq. (5) we get

$$t_{\max} = \tau \sqrt{\frac{\log(\tau_{el} \alpha_{av} I_0)}{2}}. \quad (12)$$

Figure 2 shows the Green's function for two pulse durations and two values of $I_0 \alpha_{av}$, where we fixed $\tau_{el} = 2\tau$. The peak of G vs t is always positioned after the peak of the pulse, $t_{\max} > 0$. Due to the exponential amplification, the peak of G steeply grows for larger products $I_0 \alpha_{av}$ (comparison between columns) and for longer pulses (comparison between different rows), as is well known both from numerical simulations and experiments [17]. When τ_{el} is much longer than the pulse

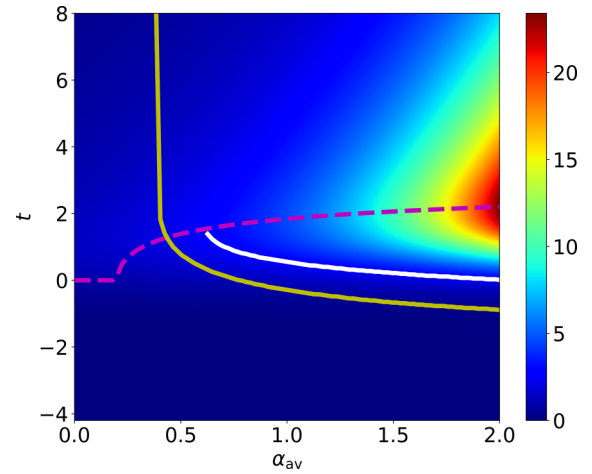


FIG. 3. Electron density n_e vs the time t (vertical axis), parameterized with respect to the avalanche coefficient α_{av} (horizontal axis). The magenta dashed line is the position of the peak given by Eq. (12). The white solid line is where the electron density becomes double the excitation due to MPI alone. The yellow solid line is the set of instants satisfying Eq. (7). The used missing parameters are $I_0 = 1$, $\alpha_N = 0.5$, $\hbar\omega = 1$, $\tau = 2$, $N = 2$, and $\tau_{el} = 5$.

duration τ (e.g., femtosecond pulses), the Green's function does not drop significantly for increasing time. On the opposite limit $\tau_{el} \ll \tau$ (e.g., nanosecond pulses), the accumulation of electrons is hindered, with the maximum of G migrating towards earlier instants; see Eq. (12).

The results of the integration of Eq. (2) for Gaussian pulses and $\alpha_N = 0.5$ are shown in Fig. 3. Comparison with full numerical simulations is discussed in Appendix B. In agreement with the shape of the Green's function, n_e first reaches a maximum after the pulse peak and then drops with a rate determined by τ_{el} . The maxima of n_e (magenta dashed line) are always placed at $t = t_{\max}$, the latter corresponding to the peak of the Green's functions, regardless of t' . With respect to α_{av} , the shape of n_e vs t does not substantially change, except for an exponential amplification. The interplay between MPI and AI can be first evaluated by finding the temporal instants where the density doubles with respect to the maximum of n_e calculated when $\alpha_{av} = 0$ (white solid line in Fig. 3). Such a condition is achieved only when α_{av} overcomes a given threshold, strongly dependent on the other parameters of the pulse. After achieving the threshold, the curve follows a hyperbola-like trend. For the sake of comparison with the theory developed above, we draw in the same graph the points where the condition defined by Eq. (7) is satisfied (yellow solid line). The two curves are almost parallel, with the theoretical prediction being slightly more stringent (i.e., AI dominance at earlier times and lower avalanche coefficients) than the numerical one.

Next, we investigate how the maximum electron density n_e^{\max} varies for different pulse durations τ and avalanche coefficients α_{av} . Typical results are shown in Fig. 4. In qualitative agreement with Eq. (10), the electron density grows exponentially with both τ and α_{av} . The transition to an avalanche-driven process, defined as a doubling of n_e as in Fig. 3, is represented by the white solid line in Fig. 4. In

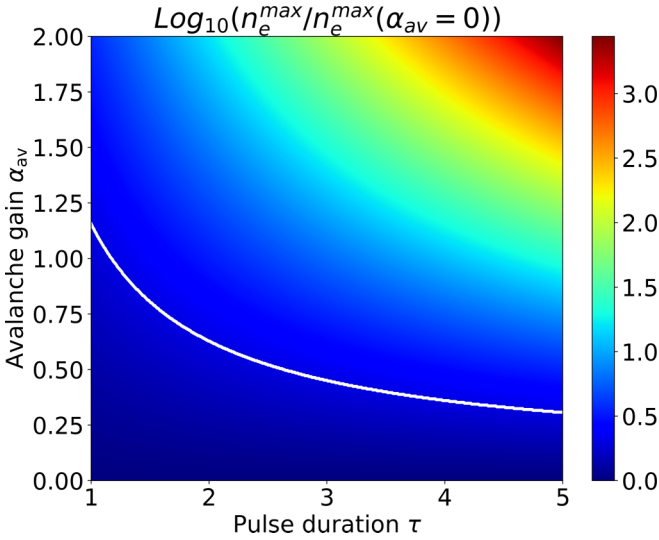


FIG. 4. Maximum of the electron density vs the AI coefficient α_{av} and the pulse duration τ for Gaussian pulses featuring $I_0 = 1$. The density are normalized with respect to the density without avalanche and plotted in logarithmic scale. The white solid line is the condition when n_e^{\max} is doubled with respect to the case $\alpha_{av} = 0$. Here we fixed $I_0 = 1$, $\alpha_N = 0.5$, $\hbar\omega = 1$, $N = 2$, and $\tau_{el} = 5$.

full analogy with Eq. (11), the curve is hyperbolic, but with a coefficient now dependent on the multiphoton order N .

V. APPLICATION TO FUSED SILICA

We now apply our model to a real case, fused silica illuminated by optical beams emitting at two different wavelengths, $\lambda = 500$ nm and $\lambda = 800$ nm. Whereas up to this point our calculations were carried out in normalized units, we now move to physical units. From Ref. [36] we take the parameters $\alpha_{av} = 4 \times 10^{-4} \text{ m}^2\text{J}^{-1}$ and $E_g = 9$ eV, in turn providing $N = 4$ at $\lambda = 500$ nm and $N = 6$ at $\lambda = 800$ nm. For the photoionization we employ the full Keldysh formula, thus accounting for the transition from MPI to TI as the impinging intensity increases [36].

A. Single pulse excitation

Figure 5 shows the corresponding maximum in the electron density vs the peak intensity I_0 for Gaussian pulses of different widths and different wavelengths. The solid lines represent the predicted value in the absence of avalanche and $\tau_{el} \rightarrow \infty$. The use of the full Keldysh formula is responsible for the abrupt changes in the distribution. In agreement with the multiphoton ionization, the slope is steeper for longer wavelength due to the larger N . When avalanche is accounted for, a sudden exponential growth in n_e is taking place. Before such a divergence, the two cases match well for long enough electron lifetime τ_{el} . Furthermore, the generation of electrons is stronger for longer pulses for a fixed peak intensity I_0 . In particular, the avalanche amplification is strongly enhanced for longer pulse durations, in agreement with the literature and Eq. (10). The dashed lines in Fig. 5 (labeled as *simplified* in each panel) is the amount of electrons generated starting from the seed induced by PI only at $t = t^*$; see Eq. (8) and Fig. 1. When

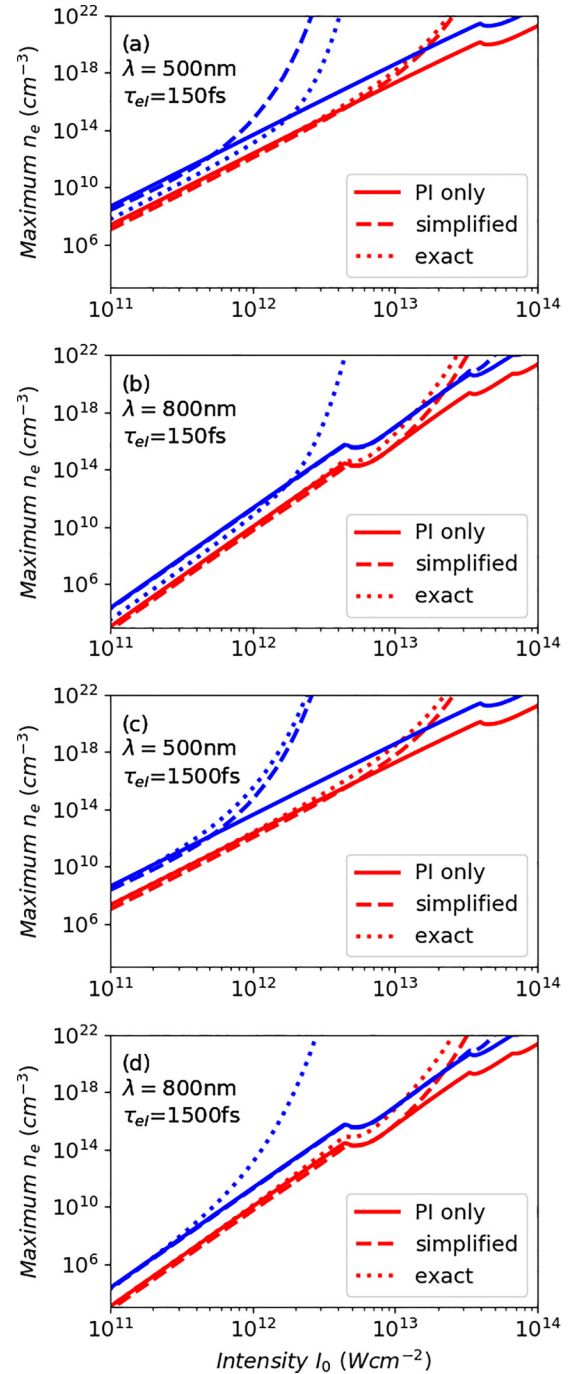


FIG. 5. Maximum of the electron density n_e vs the peak intensity I_0 in fused silica. Wavelength is 500 nm (a, c) and 800 nm (b, d). Electron lifetime τ_{el} is 150 fs (a, b) and 1.5 ps (c, d). Red and blue curves correspond to a pulse duration τ of 150 fs and 2 ps, respectively.

$\tau \ll \tau_{el}$, the exact number of excited electrons is a little bit larger, but the trend with I_0 is almost identical. When τ_{el} is shorter than the pulse duration τ , the approximation is overestimating the real amount of excited electrons. In agreement with Eq. (11), the onset of avalanche for a given peak intensity is determined by the interplay between electronic lifetime and pulse duration. In the case of Gaussian pulses, the solution of

Eq. (11) is a very good proxy for determining the transition to an avalanche-dominated regime.

B. Double pulse excitation

As a final result, we aim to apply our approach to discuss how the simultaneous illumination of the material with two pulses of different duration affects the plasma generation. Recently, the relevant role of temporal contrast in determining the modifications in bulk materials has been investigated experimentally, both in fused silica and in silicon [37,38]. We consider two pulses illuminating the sample simultaneously: a short [dubbed $I_s(t)$] and a long pulse [dubbed $I_l(t)$] with a duration of 150 fs and 10 ps, respectively. We also assume that the two pulses are perfectly synchronized by placing the peak of both pulses at $t = 0$. In applying the Keldysh formula, we simply used the sum of the two intensities: thus, we are neglecting possible coherent interference during the transitions between the excited electronic states; see, e.g., the coherent control [39]. Equation (3) provides

$$G_{\text{joint}}(t, t') = e^{\alpha_{\text{av}} \int_{t'}^t [I_s(r, \tau) + I_l(r, \tau)] d\tau} e^{-(t-t')/\tau_{\text{el}}} u_0(t - t'), \quad (13)$$

that is, the total avalanche gain is simply given by the multiplication of the separate gains, at least until Eq. (1) holds valid. The electron density is

$$n_e(t) = \int_{-\infty}^{\infty} W_{\text{PI}}(I_s + I_l) G_{\text{joint}}(t, t') dt'. \quad (14)$$

Figure 6 compares the maximum electron density achieved for different values of the peak intensities, without (top left panel) or with (top right panel) avalanche (note the different scaling on the vertical axis). The horizontal axis is the peak intensity of the short pulse $I_s(t)$, whereas each curve corresponds to a different peak intensity for the long pulse $I_l(t)$. Important to stress, here the peak intensity, which actually depends on the ratio between the pulse energy and the pulse duration, is kept fixed. We start by discussing the case without avalanche, which provides the electrons excited by direct field ionization (either MPI or TI). The joint curve differs from the case of isolated pulses only when the intensities are comparable, in agreement with the Keldysh formula. When avalanche is turned on, the exponential gain caused by the short pulse alone does not significantly change in the presence of a long pulse with an intensity I_l up to $2.0 \times 10^{-12} \text{ W cm}^{-2}$ and lower than the short pulse (see the blue and the black line in the bottom row of Fig. 6). When I_l approaches the threshold for avalanche, the exponential gain strongly differs from the gains calculated when only I_s is illuminating the material: indeed, the amplification, defined as $n_e^{\text{max}}/n_e^{\text{max}}(I_l = 0)$ and plotted in the bottom of Fig. 6, does not saturate to unity when I_s gets larger and larger. Essentially, using two pulses it is possible to decouple the plasma density from the intensity amplitude and shape, the latter being nonseparable in the case of single-pulse illumination. If the long pulse is injected earlier than the short pulse and with a delay small with respect to τ_{el} , such a scheme can be used to study the interaction between a tunable density of electrons (fixed by the long pulse, assumed to not induce permanent modifications in the material) and a short pulse of variable intensity.

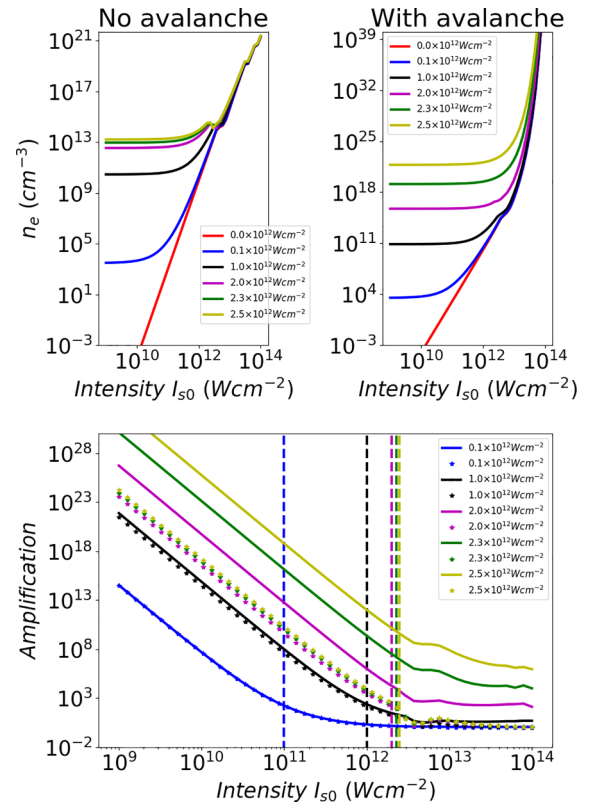


FIG. 6. Top row: Maximum of the electron density n_e in fused silica vs the peak intensity I_{s0} of the short Gaussian pulse I_s with duration 150 fs without (left side) and with (right side) avalanche. Bottom row: Ratio between the electron densities with and without the long pulse, without (symbols) or with (solid lines) avalanche. The vertical dashed lines show when the two pulses have the same peak intensity. Each color corresponds to a different peak intensity (see legend) of the long pulse with duration 10 ps. Wavelength is 800 nm and $\tau_{\text{el}} = 150$ fs.

VI. CONCLUSIONS

In conclusion, we introduced an analytical model based upon the Green's function formalism to depict the excitation of high-energy electrons in the presence of nonlinear photo-ionization (i.e., multiphoton and tunnel) and avalanche ionization. The model allows a versatile and rapid investigation of how many electrons are excited for a given optical pulse, in fact, providing a clear picture of the interplay between different ionizations and its dependence on the parameters of the optical pulse. Due to its simplicity, the model can be readily integrated in more advanced algorithms computing the optical propagation in the nonlinear regime, such as beam propagation method codes or approximated solutions based upon the variational theory. Experimentally, our model is a fast and efficient tool to describe pump-probe setups measuring the temporal dynamics of the absorption after illumination with an intense pulse [40,41]. With respect to applications, our method represents a rapid solution for estimating the best parameters to inscribe permanent structures in solids. Finally, our approach paves the way to the employment of pulse shaping to control the electron density for inputs in proximity of the onset of avalanche ionization [37].

ACKNOWLEDGMENTS

This work is supported by the Free State of Thuringia and the European Social Fund Plus (2022FGR0002), the European Union's Framework Programme for Research and Innovation Horizon 2020 under the Marie Skłodowska-Curie Grant Agreement No. 889525, and the Deutsche Forschungsgemeinschaft (CRC 1375 NOA, 398816777).

APPENDIX A: GENERALIZATION IN THE PRESENCE OF DIFFUSION

A spatial gradient in the electronic distribution yields an additional diffusion term in the rate equation

$$\frac{\partial n_e}{\partial t} = D\nabla^2 n_e + W_{\text{PI}}(I) + \left(\alpha_{\text{av}} I - \frac{1}{\tau_{el}} \right) n_e, \quad (\text{A1})$$

where the nonlinear recombination term has been neglected. Fourier transforming in space both sides of Eq. (A1) provides

$$\frac{\partial \tilde{n}_e}{\partial t} = - \left(Dk^2 + \frac{1}{\tau_{el}} \right) \tilde{n}_e + \tilde{W}_{\text{PI}} + \alpha_{\text{av}} \tilde{I} * \tilde{n}_e, \quad (\text{A2})$$

where the asterisks stands for the convolution operator and the tilde indicates the 3D spatial Fourier transform with wave vector \mathbf{k} . The electron distribution n_e is narrower than the intensity distribution I due to the dependence of W_{PI} on the power of I . For bell-shaped beams centered in $\mathbf{r} = 0$, in first approximation we can then write for the temporal Green's function

$$G(\mathbf{k}, t, t') \approx e^{\alpha_{\text{av}} \int_{t'}^t I(\mathbf{0}, \tau) d\tau} e^{-(t-t') \left(Dk^2 + \frac{1}{\tau_{el}} \right)} u_0(t-t'). \quad (\text{A3})$$

In agreement with the discussion about the electron loss rate in Ref. [17], the diffusion acts like an additional term to the electron lifetime in the excited state. Such a term depends on the spatial frequency of the harmonic: the larger the frequency, the shorter the effective lifetime becomes.

APPENDIX B: VERIFICATION VERSUS NUMERICAL SIMULATIONS

We verified the correctness of our solutions based upon the Green formalism by simulating Eq. (1) using a second-order Runge-Kutta method. We test the validity of Eqs. (2) and (3) by comparing numerical and theoretical results both for rectangular and Gaussian waveforms. Figure 7 shows the comparison between theory and numerical simulations in the case of a square pulse: the agreement is perfect within the numerical accuracy, hence confirming the validity of our analytical results. Next we checked the validity in the case of a Gaussian pulse, the comparison being plotted in Fig. 8. The theoretical and numerical simulations are once again in agreement for different values of the parameters, thus confirming the validity of the Green's function method for the Gaussian case plotted in Fig. 2.

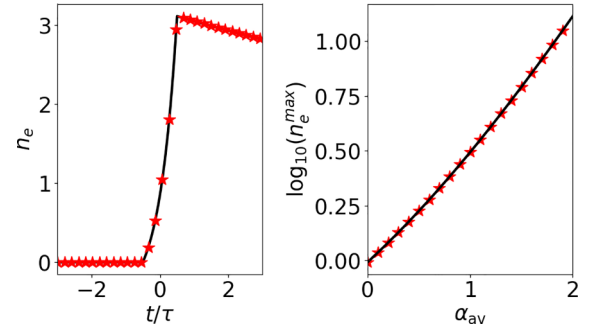


FIG. 7. Comparison between theoretical (black solid lines) and numerical results (red stars) in the case of square pulses. Left side: n_e vs time t for $\alpha_{\text{av}} = 1$. Right side: Logarithm of n_e^{max} [see Eq. (10)] vs the avalanche gain α_{av} . The employed parameters are $I_0 = 1$, $\hbar\omega = 1$, $\tau = 2$, $N = 2$, and $\tau_{el} = 50$.

APPENDIX C: ROLE OF THE NONLINEAR RECOMBINATION TERM

From Eq. (1), the nonlinear recombination term $-\sigma n_e^2$ is half the amplitude of the linear one $-n_e/\tau_{el}$ when

$$n_e^{\text{max}} = \frac{1}{2\sigma\tau_{el}}. \quad (\text{C1})$$

Thus, the nonlinear recombination term is expected to become relevant once the electron distribution overcomes such a threshold. We verified such idea by solving numerically Eq. (1) for $\sigma \neq 0$ and comparing the density profile with the results provided by our Green's function method. The comparison is provided in Fig. 9 in the case of Gaussian pulses. In the top panel n_e^{max} is plotted vs the pulse duration τ for two different values of the avalanche factor, thus sharing the same threshold. Incidentally, for $\sigma = 0$ the peak n_e^{max} can be directly computed as an integral using Eq. (2) and the condition (12). As predicted, the two solutions start to diverge once the threshold is overcome, that is, once the electron density becomes large enough. The nonlinear recom-

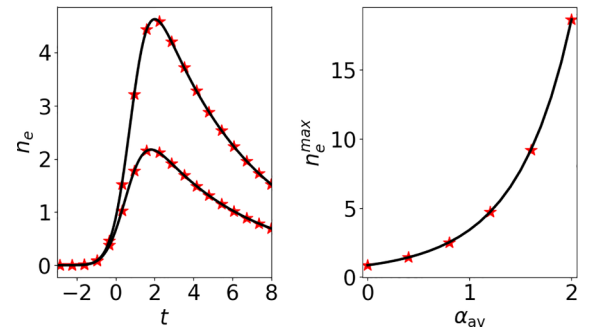


FIG. 8. Comparison between theoretical (black solid lines) and numerical results (red stars) in the case of Gaussian pulses. Left side: n_e vs time t for $\alpha_{\text{av}} = 1$ (lower curve) and $\alpha_{\text{av}} = 1.5$ (upper curve) with $\tau = 2$ and $\tau_{el} = 50$. Right side: n_e^{max} vs the avalanche gain α_{av} for $\tau = 2$ and $\tau_{el} = 50$. The remaining parameters are $I_0 = 1$, $\hbar\omega = 1$, and $N = 2$.

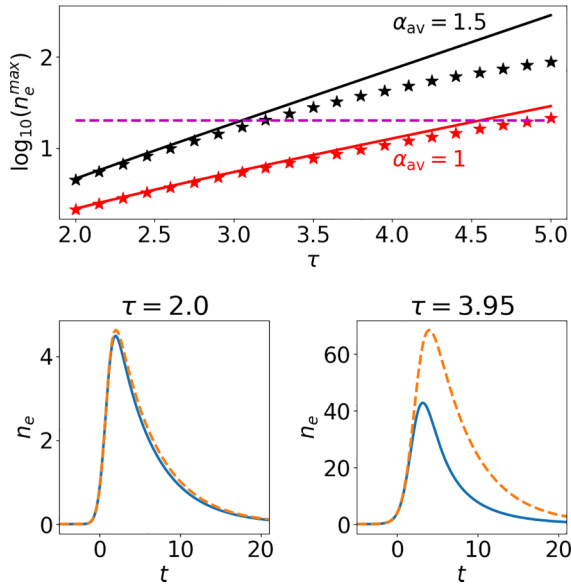


FIG. 9. Interplay between linear and nonlinear recombination terms for Gaussian pulses. Top panel: n_e^{\max} vs the pulse duration for $\sigma = 0$ (solid lines) and for $\sigma = 0.005$ (symbols). The dashed horizontal line is the transition value provided by (C1). Bottom: Electron density n_e vs the time t for $\sigma = 0$ (blue solid lines) and for $\sigma = 0.005$ (orange dashed lines); here $\alpha_{av} = 1.5$ and the pulse duration τ is reported in the title of each panel. In all panels we took $I_0 = 1$, $\alpha_N = 1$, $\tau_{el} = 5$, $N = 2$, and $\hbar\omega = 1$.

bination becomes more relevant for longer pulses, the latter favoring the avalanche ionization as discussed in the main text. Looking at the temporal evolution of n_e , the nonlinear recombination fixes the density to a given value, after which the electron distribution relaxes with a time constant τ_{el} .

The threshold value n_e^{th} can be found by setting the temporal derivative of n_e equal to zero; recalling Eq. (5), Eq. (1)

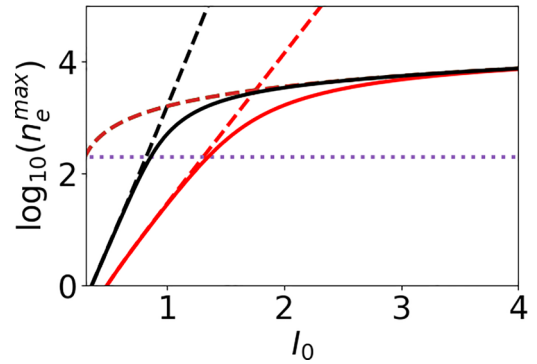


FIG. 10. Maximum electron density n_e^{\max} vs the peak intensity I_0 in the case of Gaussian pulses of duration $\tau = 5$ (red curves) and 10 (black curves). Dashed and solid lines are the results for $\sigma = 0$ and $\sigma = 5 \times 10^{-4}$. The brown dashed line is Eq. (C2). The dotted horizontal line is Eq. (C1). In all panels $\alpha_{av} = 1$, $\alpha_N = 1$, $\tau_{el} = 5$, $N = 2$, and $\hbar\omega = 1$.

then provides

$$n_e^{\text{th}} = \frac{I/I(t_{\max}) - 1}{2\sigma\tau_{el}} \left[1 \pm \sqrt{1 + \frac{4\sigma\tau_{el}^2 W_{\text{PI}}}{[I/I(t_{\max}) - 1]^2}} \right], \quad (\text{C2})$$

where the sign is plus when $I > I(t_{\max})$, and minus otherwise. For large intensities we obtain $n_e^{\text{th}} \approx \frac{\alpha_{av} I}{\sigma}$: the clamping value is inversely proportional to σ as expected.

Given that Eq. (C2) is monotonic vs the intensity I , we can safely change it with I_0 in the case of isolated Gaussian pulses. The maximum of the electron density vs the input intensity is plotted in Fig. 10. For I small enough to match the condition $n_e^{\max} < 1/(2\sigma\tau_{el})$, the full numerical simulations match our approach based upon the Green's function, that is, nonlinear recombination is negligible. When the condition (C1) is satisfied (dotted horizontal line in Fig. 10), the numerical simulations bend away from the Green's function solution, finally converging to the clamping value n_e^{th} provided by Eq. (C2).

[1] P. B. Corkum, Plasma perspective on strong field multiphoton ionization, *Phys. Rev. Lett.* **71**, 1994 (1993).
 [2] A. S. Disa, T. F. Nova, and A. Cavalleri, Engineering crystal structures with light, *Nat. Phys.* **17**, 1087 (2021).
 [3] S.-I. Chu and D. A. Telnov, Beyond the Floquet theorem: Generalized Floquet formalisms and quasienergy methods for atomic and molecular multiphoton processes in intense laser fields, *Phys. Rep.* **390**, 1 (2004).
 [4] T. Oka and S. Kitamura, Floquet engineering of quantum materials, *Annu. Rev. Condens. Matter Phys.* **10**, 387 (2019).
 [5] E. Goulielmakis and T. Brabec, High harmonic generation in condensed matter, *Nat. Photon.* **16**, 411 (2022).
 [6] H. Lakhotia, H. Kim, M. Zhan, S. Hu, S. Meng, and E. Goulielmakis, Laser picoscopy of valence electrons in solids, *Nature (London)* **583**, 55 (2020).
 [7] O. Neufeld, N. Tancogne-Dejean, H. Hübener, U. De Giovannini, and A. Rubio, Are there universal signatures of topological phases in high-harmonic generation? Probably not. *Phys. Rev. X* **13**, 031011 (2023).

[8] R. R. Gattass and E. Mazur, Femtosecond laser micromachining in transparent materials, *Nature Photon* **2**, 219 (2008).
 [9] A. Tünnermann, C. Momma, and S. Nolte, Perspective on ultrashort pulse laser micromachining, *Appl. Phys. A* **129**, 157 (2023).
 [10] Y. P. Raïzer, Breakdown and heating of gases under the influence of a laser beam, *Sov. Phys. Usp.* **8**, 650 (1966).
 [11] Y.-R. Shen, *Principles of Nonlinear Optics* (Wiley, New York, 1984).
 [12] M. Geissler, G. Tempea, A. Scrinzi, M. Schnürer, F. Krausz, and T. Brabec, Light propagation in field-ionizing media: Extreme nonlinear optics, *Phys. Rev. Lett.* **83**, 2930 (1999).
 [13] V. Nathan, A. H. Guenther, and S. S. Mitra, Review of multiphoton absorption in crystalline solids, *J. Opt. Soc. Am. B* **2**, 294 (1985).
 [14] M. Sparks, D. L. Mills, R. Warren, T. Holstein, A. A. Maradudin, L. J. Sham, E. Loh, and D. F. King, Theory of electron-avalanche breakdown in solids, *Phys. Rev. B* **24**, 3519 (1981).

- [15] T. Otobe, Wavelength dependence of the laser-excitation process on a silicon surface, *Phys. Rev. Appl.* **13**, 024062 (2020).
- [16] N. Kroll and K. M. Watson, Theoretical study of ionization of air by intense laser pulses, *Phys. Rev. A* **5**, 1883 (1972).
- [17] P. K. Kennedy, A first-order model for computation of laser-induced breakdown thresholds in ocular and aqueous media. I. Theory, *IEEE J. Quantum Electron.* **31**, 2241 (1995).
- [18] L. Sudrie, A. Couairon, M. Franco, B. Lamouroux, B. Prade, S. Tzortzakis, and A. Mysyrowicz, Femtosecond laser-induced damage and filamentary propagation in fused silica, *Phys. Rev. Lett.* **89**, 186601 (2002).
- [19] V. Y. Fedorov, M. Chanal, D. Grojo, and S. Tzortzakis, Accessing extreme spatiotemporal localization of high-power laser radiation through transformation optics and scalar wave equations, *Phys. Rev. Lett.* **117**, 043902 (2016).
- [20] B. C. Stuart, M. D. Feit, A. M. Rubenchik, B. W. Shore, and M. D. Perry, Laser-induced damage in dielectrics with nanosecond to subpicosecond pulses, *Phys. Rev. Lett.* **74**, 2248 (1995).
- [21] M. Li, S. Menon, J. P. Nibarger, and G. N. Gibson, Ultrafast electron dynamics in femtosecond optical breakdown of dielectrics, *Phys. Rev. Lett.* **82**, 2394 (1999).
- [22] L. V. Keldysh, Ionization in the field of a strong electromagnetic wave, *Sov. Phys. JETP* **20**, 1307 (1965).
- [23] C. B. Schaffer, A. Brodeur, and E. Mazur, Laser-induced breakdown and damage in bulk transparent materials induced by tightly focused femtosecond laser pulses, *Meas. Sci. Technol.* **12**, 1784 (2001).
- [24] Y. Shen, Self-focusing: Experimental, *Prog. Quantum Electron.* **4**, 1 (1975).
- [25] B. Rethfeld, Free-electron generation in laser-irradiated dielectrics, *Phys. Rev. B* **73**, 035101 (2006).
- [26] G. D. Tsibidis and E. Stratakis, Ionization dynamics and damage conditions in fused silica irradiated with mid-infrared femtosecond pulses, *Appl. Phys. Lett.* **122**, 043501 (2023).
- [27] Q. Feng, J. Moloney, A. Newell, E. Wright, K. Cook, P. Kennedy, D. Hammer, B. Rockwell, and C. Thompson, Theory and simulation on the threshold of water breakdown induced by focused ultrashort laser pulses, *IEEE J. Quantum Electron.* **33**, 127 (1997).
- [28] M. Lamperti, V. Jukna, O. Jedrkiewicz, P. Di Trapani, R. Stoian, T. E. Itina, C. Xie, F. Courvoisier, and A. Couairon, Invited Article: Filamentary deposition of laser energy in glasses with Bessel beams, *APL Photonics* **3**, 120805 (2018).
- [29] G. Arfken and H. Weber, *Mathematical Methods for Physicists* (Academic Press, Amsterdam, 2001).
- [30] E. Galiffi, R. Tirole, S. Yin, H. Li, S. Vezzoli, P. A. Huidobro, M. G. Silveirinha, R. Sapienza, A. Alù, and J. B. Pendry, Photonics of time-varying media, *Adv. Photon.* **4**, 014002 (2022).
- [31] R. Tirole, S. Vezzoli, E. Galiffi, I. Robertson, D. Maurice, B. Tilmann, S. A. Maier, J. B. Pendry, and R. Sapienza, Double-slit time diffraction at optical frequencies, *Nat. Phys.* **19**, 999 (2023).
- [32] P. P. Rajeev, M. Gertsvolf, P. B. Corkum, and D. M. Rayner, Field dependent avalanche ionization rates in dielectrics, *Phys. Rev. Lett.* **102**, 083001 (2009).
- [33] C. Conti, M. A. Schmidt, P. S. J. Russell, and F. Biancalana, Highly noninstantaneous solitons in liquid-core photonic crystal fibers, *Phys. Rev. Lett.* **105**, 263902 (2010).
- [34] J. D. Hunter, Matplotlib: A 2D graphics environment, *Comput. Sci. Eng.* **9**, 90 (2007).
- [35] C. R. Harris, K. J. Millman, S. J. van der Walt, R. Gommers, P. Virtanen, D. Cournapeau, E. Wieser, J. Taylor, S. Berg, N. J. Smith *et al.*, Array programming with NumPy, *Nature (London)* **585**, 357 (2020).
- [36] A. Couairon, L. Sudrie, M. Franco, B. Prade, and A. Mysyrowicz, Filamentation and damage in fused silica induced by tightly focused femtosecond laser pulses, *Phys. Rev. B* **71**, 125435 (2005).
- [37] A. Wang, A. Das, and D. Grojo, Temporal-contrast imperfections as drivers for ultrafast laser modifications in bulk silicon, *Phys. Rev. Res.* **2**, 033023 (2020).
- [38] Y. Lei, H. Wang, G. Shayeganrad, Y. Svirko, and P. G. Kazansky, Controlling ultrafast laser writing in silica glass by pulse temporal contrast, [arXiv:2401.09055](https://arxiv.org/abs/2401.09055).
- [39] Y. Silberberg, Quantum coherent control for nonlinear spectroscopy and microscopy, *Annu. Rev. Phys. Chem.* **60**, 277 (2009).
- [40] K. Bergner, B. Seyfarth, K. A. Lammers, T. Ullsperger, S. Döring, M. Heinrich, M. Kumkar, D. Flamm, A. Tünnermann, and S. Nolte, Spatio-temporal analysis of glass volume processing using ultrashort laser pulses, *Appl. Opt.* **57**, 4618 (2018).
- [41] P. Jürgens, M. J. J. Vrakking, A. Husakou, R. Stoian, and A. Mermillod-Blondin, Plasma formation and relaxation dynamics in fused silica driven by femtosecond short-wavelength infrared laser pulses, *Appl. Phys. Lett.* **115**, 191903 (2019).